

ADVANCED MATERIALS

Supporting Information

for *Adv. Mater.*, DOI 10.1002/adma.202313511

Gold-Template-Assisted Mechanical Exfoliation of Large-Area 2D Layers Enables Efficient and Precise Construction of Moiré Superlattices

Kang Wu, Hao Wang, Meng Yang, Li Liu, Zhenyu Sun, Guojing Hu, Yanpeng Song, Xin Han, Jiangang Guo, Kehui Wu, Baojie Feng, Chengmin Shen, Yuan Huang, Youguo Shi, Zhigang Cheng, Haitao Yang, Lihong Bao*, Sokrates T. Pantelides and Hong-Jun Gao*

Supporting Information

Gold-template-assisted Mechanical Exfoliation of Large-area 2D layers Enables Efficient and Precise Construction of Moiré Superlattices

Kang Wu, Hao Wang, Meng Yang, Li Liu, Zhenyu Sun, Guojing Hu, Yanpeng Song, Xin Han, Jiangang Guo, Kehui Wu, Baojie Feng, Chengmin Shen, Yuan Huang, Youguo Shi, Zhigang Cheng, Haitao Yang, Lihong Bao*, Sokrates T. Pantelides, Hong-Jun Gao*

Contents:

Figures S1 to S22

Tables S1 to S2

Supplementary Notes

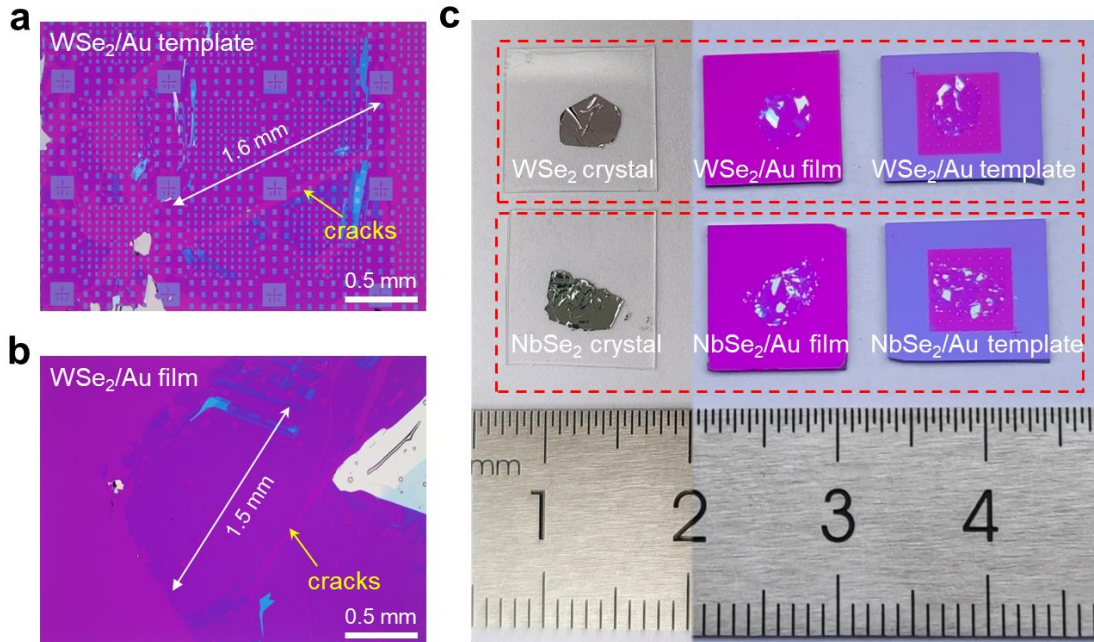


Figure S1. Optical images of large-area WSe₂ and NbSe₂ layers exfoliated on Au-film substrate and on Au-template substrate. **a,b**, Optical images of large-area WSe₂ monolayers on Au-template substrates using our Au-template-assisted exfoliation method (**a**) and on Au-film substrates using the Au-assisted exfoliation method (**b**). The maximum size of continuously atomically thin layers achievable on the Au-template substrates reaches a millimeter scale (**a**), which is comparable with the maximum size achievable on the Au-film substrates (**b**). **c**, Macroscopic optical images of WSe₂ and NbSe₂ crystals on PDMS for exfoliation, exfoliated large-area WSe₂ and NbSe₂ layers on both Au-film substrate and Au-template substrate. The macroscopic size of exfoliated 2D layers is almost the same as the size of the bulk crystals for both our Au-template-assisted exfoliation method and the Au-assisted exfoliation method.

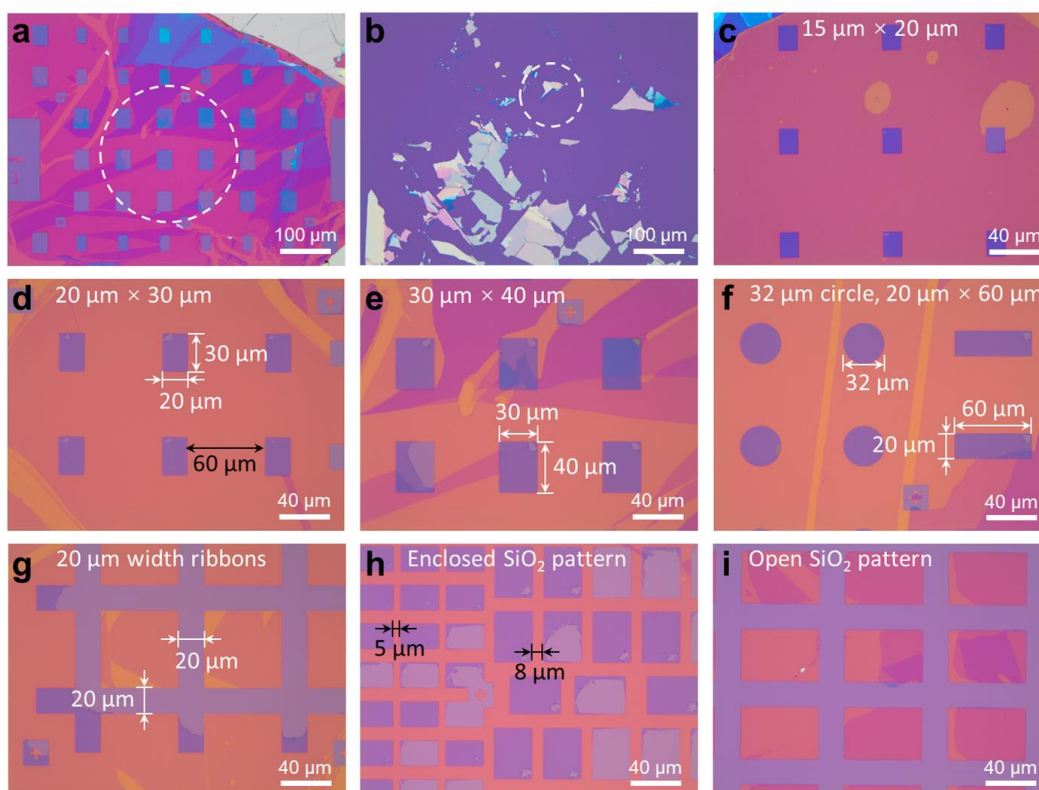


Figure S2. Optical images of exfoliated monolayer MoS₂ on different Au-patterned SiO₂ substrates.

a,b, Comparison of the exfoliation effect of the Au-template-assisted exfoliation method (using Au-patterned SiO₂ substrates) and conventional Scotch-tape exfoliation method (using normal SiO₂ substrates). Using the Au-patterned SiO₂ substrates, the sizes of monolayer MoS₂ reaches up to 30 × 40 square microns on the rectangular SiO₂ surfaces, while using normal SiO₂ substrates, the length of monolayer MoS₂ only reaches a few microns, as marked by the white dashed circles in **(a,b)**. **c-g**, Optical images of exfoliated monolayer MoS₂ on different Au-patterned SiO₂ substrates with patterns of different shapes and sizes, including rectangles with sizes of 15 × 20 μm² **(c)**, rectangles with sizes of 20 × 30 μm² **(d)**, rectangles with sizes of 30 × 40 μm² **(e)**, circles with a diameter of 32 μm **(f)**, ribbons with a width of 20 μm **(g)**. **h**, Optical images of exfoliated monolayer MoS₂ on Au-patterned substrates with denser SiO₂ rectangles. The distance between adjacent rectangles is reduced from 60 μm **(d)** to less than 10 μm **(h)**, and the ratio of exposed SiO₂ over the entire Au-patterned substrate is increased from ~10% **(d)** to ~60% **(h)**. **i**, Optical image of exfoliated monolayer MoS₂ on Au-patterned substrates with open SiO₂ patterns. The shape of Au film is rectangle, while the exposed SiO₂ is continuous around rectangular Au film.

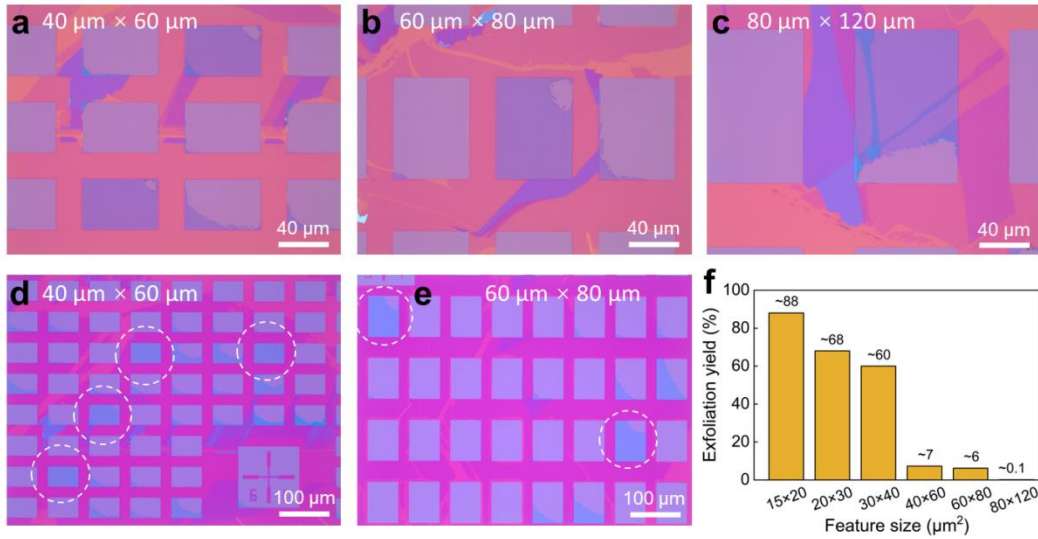


Figure S3. Optical images of exfoliated monolayer MoS₂ on Au-patterned SiO₂ substrates with enlarged sizes of SiO₂ rectangles. a-e, Optical images of exfoliated monolayer MoS₂ on Au-patterned SiO₂ substrates with feature sizes of 40 × 60 μm² (a,d), 60 × 80 μm² (b,e), and 80 × 120 μm² (c), respectively. f, The influence of feature sizes of SiO₂ rectangles on the exfoliation yield of MoS₂. The exfoliation yield is defined as the ratio of the number of SiO₂ rectangles covered almost completely by monolayer MoS₂ (as indicated by the white dashed circles in (d) and (e)) to the total number of SiO₂ rectangles in between which the Au film is covered by continuous MoS₂ layers.

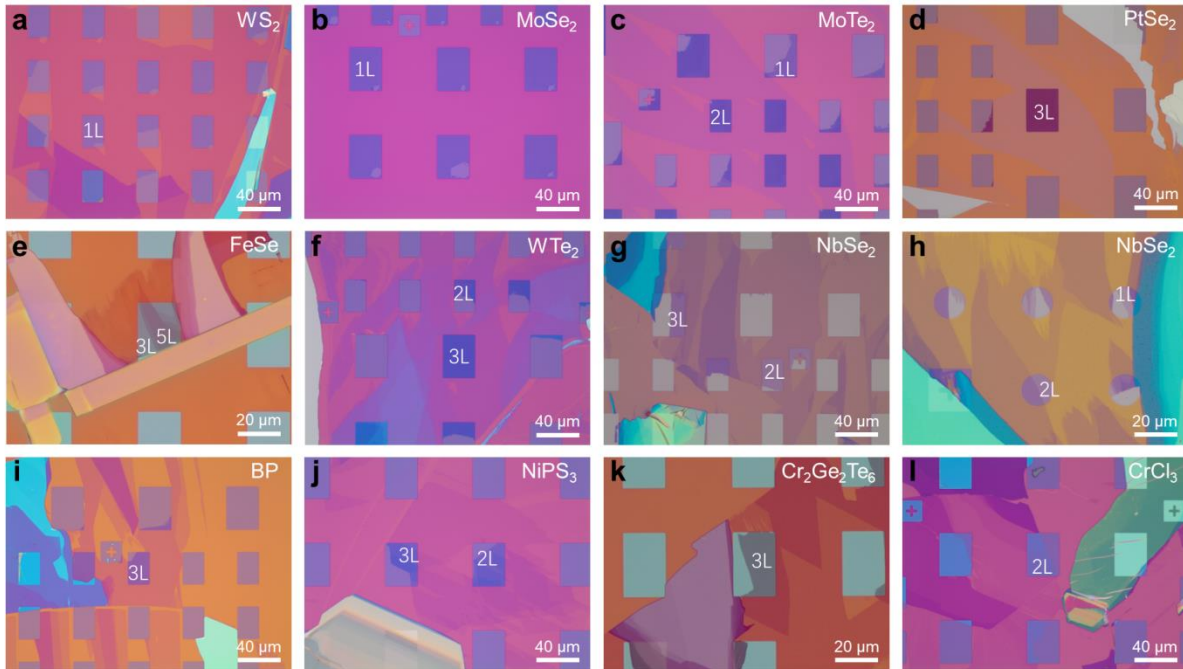


Figure S4. Optical images of large-area 2D atomically thin crystals obtained by the Au-template-assisted exfoliation method. a-e, Optical images of exfoliated large-area 2D atomically thin crystals that are not mentioned in the main text, including WS_2 , MoSe_2 , MoTe_2 , PtSe_2 , and FeSe . f-l, Supplementary optical images of exfoliated large-area 2D atomically thin crystals that are mentioned in the main text, including WTe_2 , NbSe_2 , BP, NiPS_3 , $\text{Cr}_2\text{Ge}_2\text{Te}_6$, and CrCl_3 .

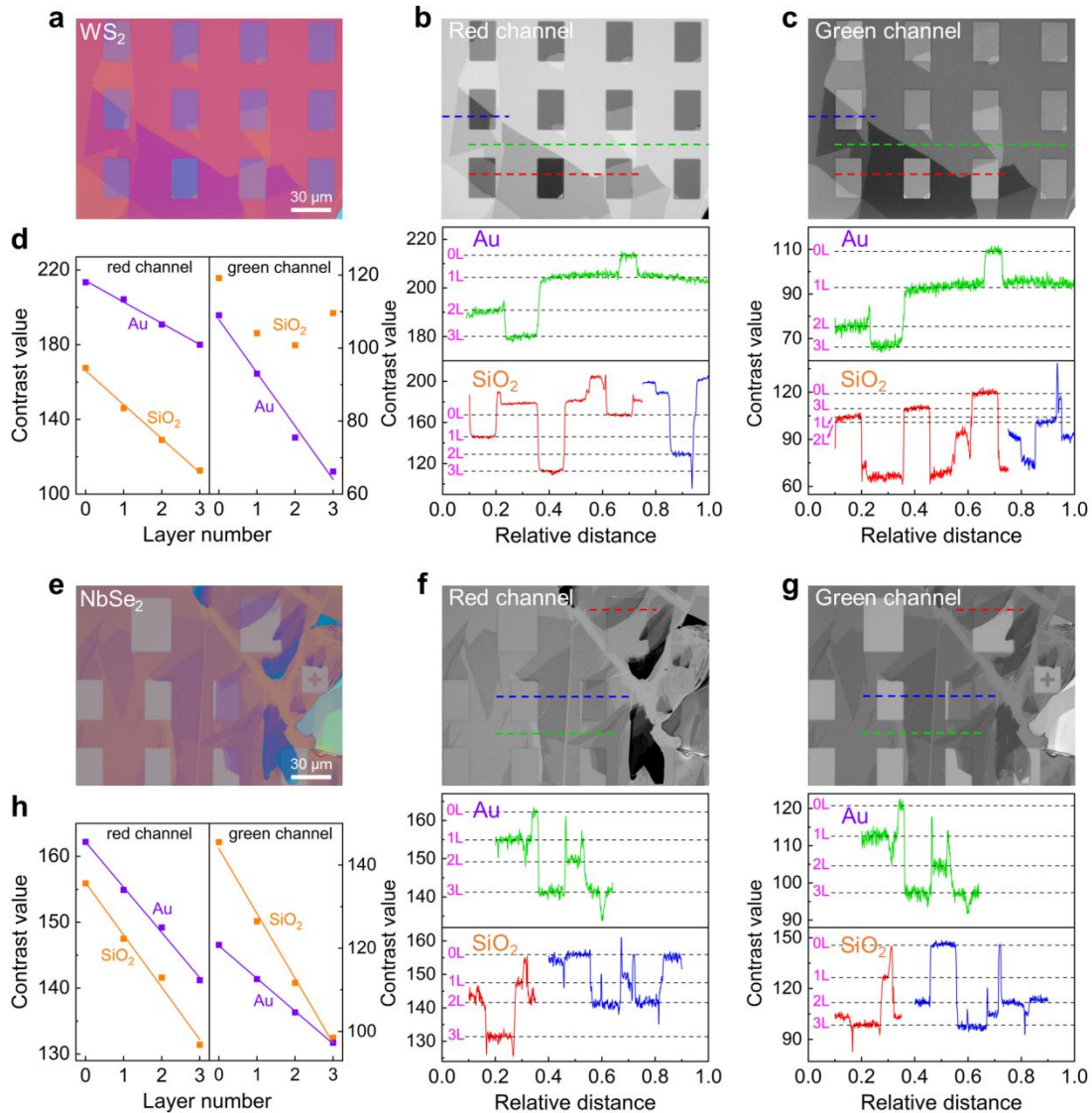


Figure S5. Layer number identification of exfoliated atomically thin WS_2 and NbSe_2 crystals on Au-patterned SiO_2 substrates by optical contrast. **a**, An optical image of exfoliated WS_2 layers. **b,c**, Grayscale images of the red and green channels of sample in **(a)**, along with the corresponding contrast value profiles along the red, blue, and green dashed lines. **d**, Layer-number dependence of contrast values of WS_2 layers on both rectangular SiO_2 substrates and Au films extracted from the contrast value profiles in **(b,c)**. **e**, An optical image of exfoliated NbSe_2 layers. **f,g**, Grayscale images of the red and green channels of sample in **(e)**, along with the corresponding contrast value profiles along the red, blue, and green dashed lines. **h**, Layer-number dependence of contrast values of NbSe_2 layers on both rectangular SiO_2 substrates and Au films extracted from the contrast value profiles in **(f,g)**. For grayscale images of red and green channels, the contrast values of WS_2 and NbSe_2 layers on both rectangular SiO_2 substrates

and Au film have approximately linear relationships with the layer number (except for green channel of WS₂ layers on SiO₂ substrate^[1]), which confirms our previous estimation of corresponding layer numbers (monolayer, bilayer, and trilayer).

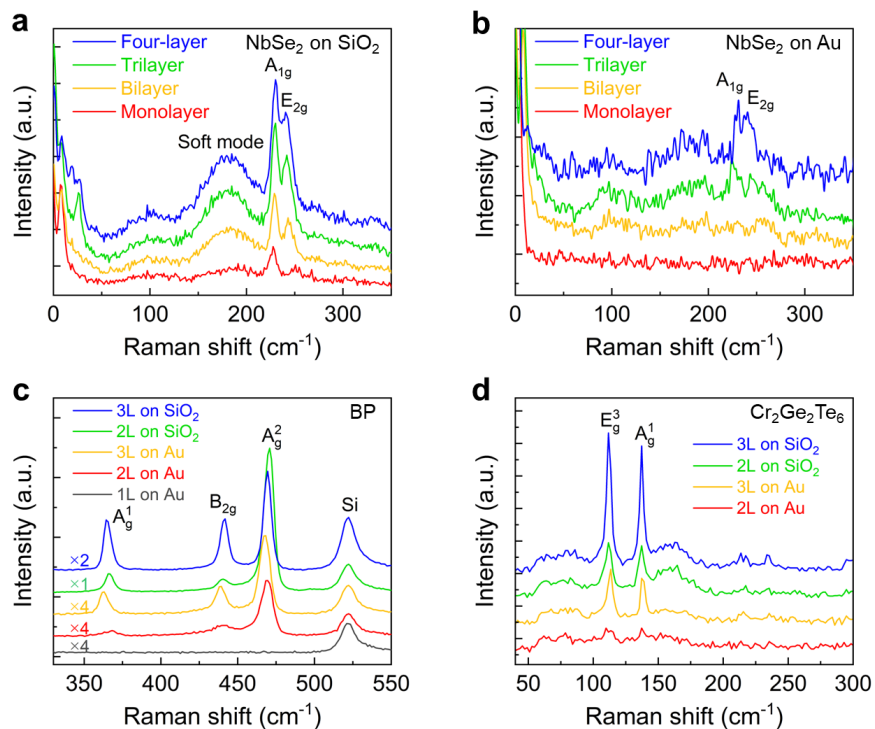


Figure S6. Raman spectra of exfoliated atomically thin NbSe₂, BP, and Gr₂Ge₂Te₆ layers. **a,b**, Raman spectra of monolayer to four-layer NbSe₂ on rectangular SiO₂ substrates (**a**) and Au films (**b**). Two characteristic peaks, A_{1g} and E_{2g}, and soft modes are clearly observed for all monolayer to four-layer NbSe₂ on SiO₂ substrates. However, for NbSe₂ on Au substrates, the A_{1g} and E_{2g} peaks of monolayer and bilayer NbSe₂ are indistinguishable, while the E_{2g} and A_{1g} peaks of trilayer and four-layer NbSe₂ can be discerned but with lower signal-to-noise ratios. The successful exfoliation of monolayer to few-layer NbSe₂ on exposed rectangular SiO₂ substrates enables us to investigate the layer-dependent Raman characteristics of atomically thin NbSe₂. From monolayer to four-layer NbSe₂, the A_{1g} peak exhibits a blue shift, with its position changing from 227.9 cm⁻¹ to 230.1 cm⁻¹. On the contrary, the E_{2g} peak displays a red shift, with its position changing from 250.6 cm⁻¹ to 240.5 cm⁻¹, which is consistent with previous results^[2]. **c**, Raman spectra of atomically thin BP. Three characteristic peaks, A_{1g}¹, B_{2g}, and A_{2g}² are

observed for bilayer and trilayer BP on both SiO_2 substrates and Au films, and the Raman signals of samples on SiO_2 substrates are several times stronger than those on Au films. For bilayer BP, the intensity of A_g^2 peak is disproportionately high compared with A_g^1 and B_{2g} peaks. Furthermore, the frequencies of A_g^1 and A_g^2 peaks in bilayer samples are higher than those in trilayer samples. These characteristics of bilayer BP are consistent with a previous report^[3]. **d**, Raman spectra of atomically thin $\text{Cr}_2\text{Ge}_2\text{Te}_6$. For bilayer $\text{Cr}_2\text{Ge}_2\text{Te}_6$ on Au film, the characteristic peaks, E_g^3 and A_g^1 , are comparable with the noise, while for bilayer $\text{Cr}_2\text{Ge}_2\text{Te}_6$ on SiO_2 substrate, improved signal-to-noise ratio is observed. The Raman results of $\text{Cr}_2\text{Ge}_2\text{Te}_6$ also prove that SiO_2 substrates are more suitable for observing optical signals of 2D layers than Au films.

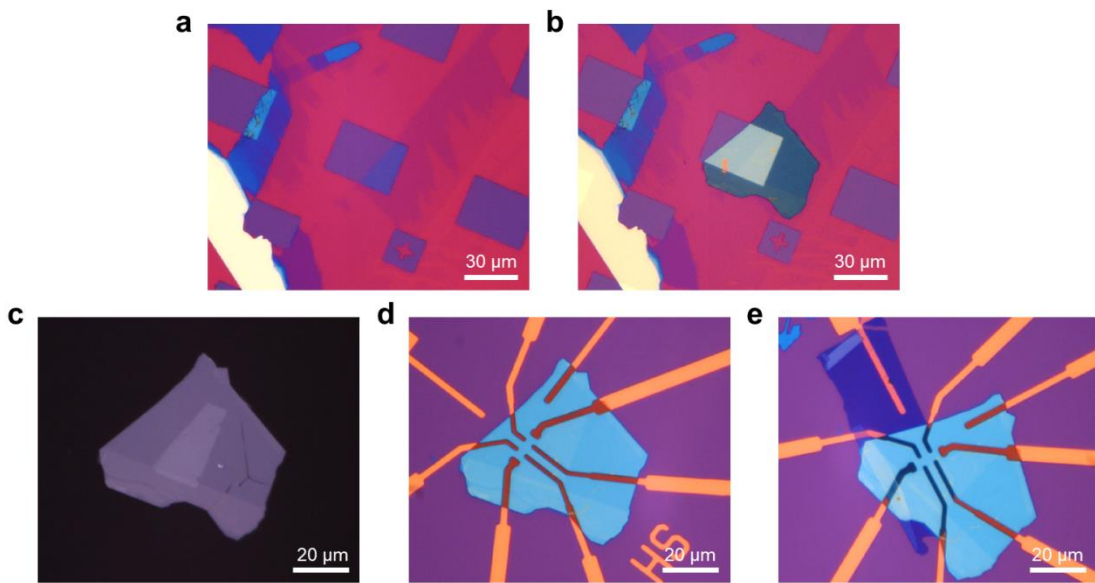


Figure S7. Optical images taken at different stages of device fabrication of a bilayer BP top-gated FET.

a, The exfoliation of bilayer BP on Au-patterned SiO_2 substrate. **b**, The deposition of a thin hBN layer on BP. Then, the hBN-capped bilayer BP is carefully picked up using a PPC/PDMS stamp mounted on a glass slide. **c**, The bilayer BP/hBN/PPC/PDMS stack. The bilayer BP remains completely intact on hBN after the pick-up. **d**, The bilayer BP/hBN stack are slowly released onto pre-patterned Cr/Au (3 nm/18 nm) contact electrodes. **e**, The bilayer BP top-gated FET are successfully fabricated after the deposition of thin graphite serving as the top gate electrode.

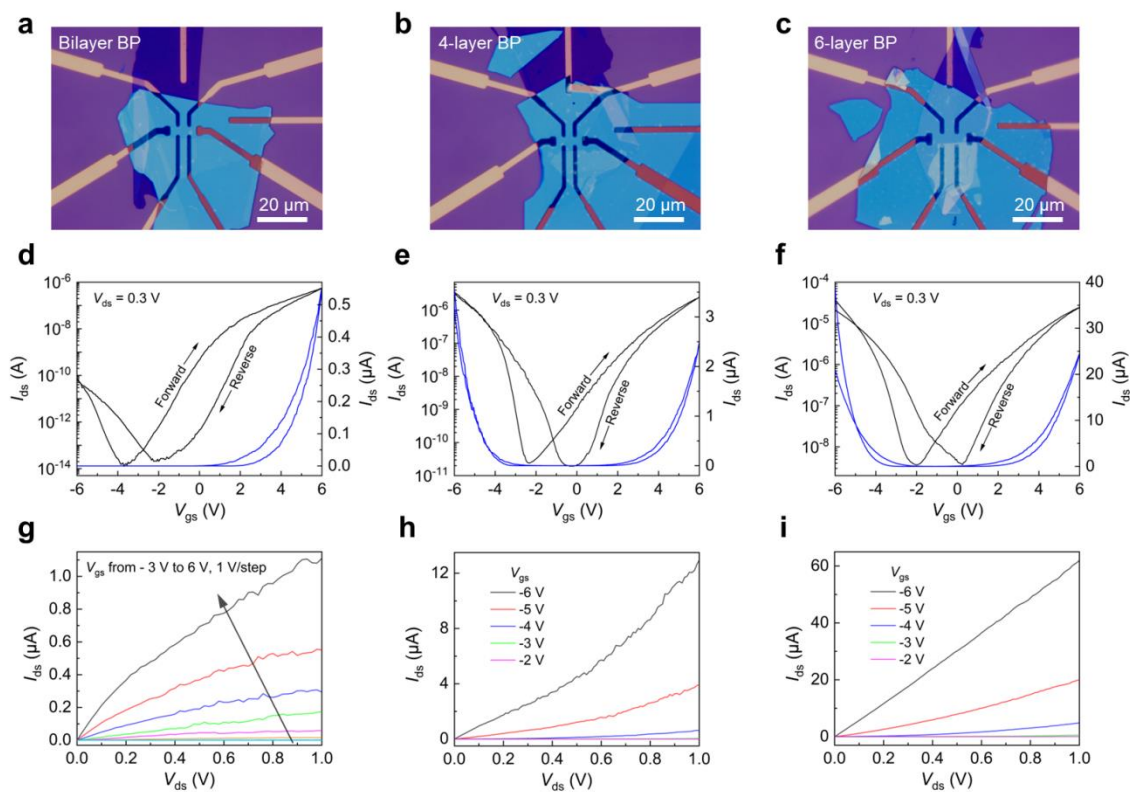


Figure S8. Electrical transport properties of bilayer, four-layer, and six-layer BP top-gated FETs. a-c, Optical images of bilayer (a), four-layer (b), and six-layer (c) BP top-gated FETs with pre-patterned Cr/Au (3 nm/18 nm) serving as contact electrodes and transferred graphite serving as the top gate electrode. d-f, Transfer characteristics of the bilayer (d), four-layer (e), and six-layer (f) BP top-gated FETs at $V_{ds} = 0.3$ V in linear (blue line) and logarithmic (black line) scales. The observed hysteresis may be attributed to the influence of the dielectric environment from SiO_2 substrates. g-i, Output characteristics of the bilayer (g), four-layer (h), and six-layer (i) BP top-gated FETs at V_{ds} range from 0 to 1 V. The gate voltage V_g is from -3 V to 6 V with a step of 1 V for bilayer FET and -6 V to -2 V with a step of 1 V for four-layer and six-layer FETs.

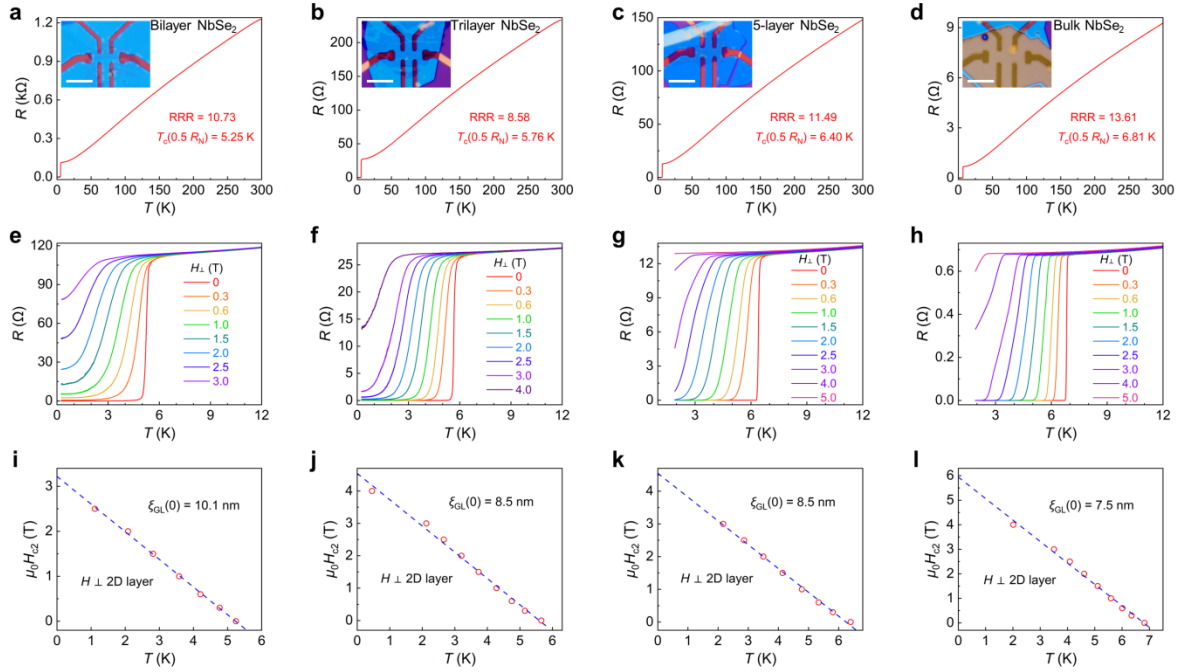


Figure S9. Electrical transport properties of bilayer, trilayer, five-layer, and bulk NbSe₂ Hall devices. **a-d**, Temperature-dependent resistance of bilayer (**a**), trilayer (**b**), five-layer (**c**), and bulk (**d**) NbSe₂ Hall devices. Insets in a-d: optical images of the corresponding NbSe₂ Hall devices with pre-patterned Cr/Au (3 nm/18 nm) contact electrodes. **e-h**, Temperature-dependent resistance of the bilayer (**e**), trilayer (**f**), five-layer (**g**), and bulk (**h**) NbSe₂ Hall devices under different out-of-plane magnetic fields. The temperature range is from 0.2 K to 300 K for bilayer and trilayer devices, and from 1.9 K to 300 K for five-layer and bulk devices. **i-l**, Temperature dependence of the upper critical field H_{c2} for the bilayer (**i**), trilayer (**j**), five-layer (**k**), and bulk (**l**) NbSe₂ Hall devices. The blue dashed lines are the linear fittings. The extracted in-plane GL coherence length at zero temperature $\xi_{GL}(0)$ increased from 7.5 nm to 10.1 nm as the thickness of NbSe₂ is reduced from bulk to bilayer.

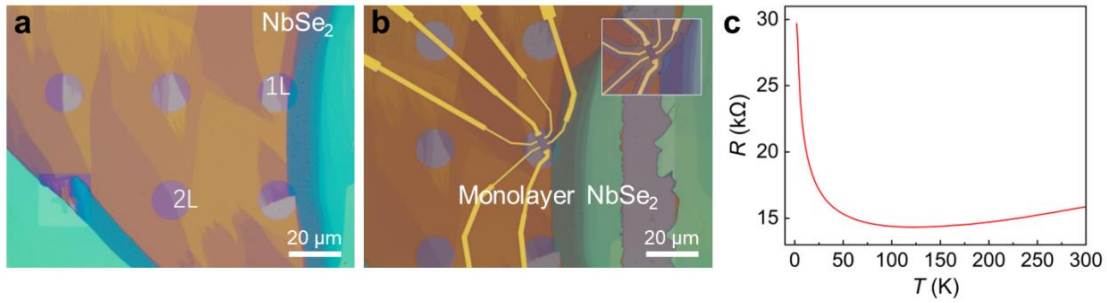


Figure S10. Monolayer NbSe₂ Hall device. **a**, Optical image of exfoliated monolayer NbSe₂ on Au-patterned SiO₂ substrate. **b**, Optical image of the fabricated monolayer NbSe₂ Hall device after EBL and EBD processes. The inset is the final device after a second EBL process and a dry etching process of Au. **c**, Temperature-dependent resistance of the monolayer NbSe₂ Hall device.

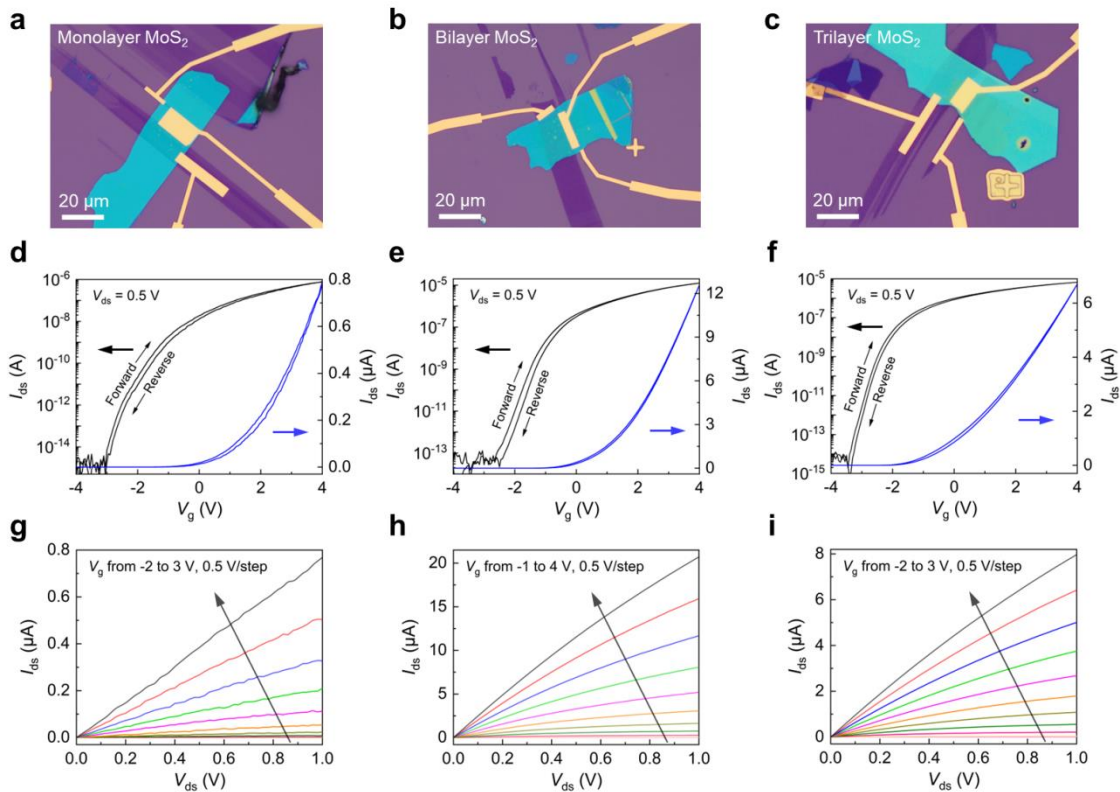


Figure S11. Electrical transport properties of monolayer, bilayer, and trilayer MoS₂ top-gated FETs. **a-c**, Optical images of monolayer (a), bilayer (b), and trilayer (c) MoS₂ top-gated FETs with thin graphite as

contact electrodes. **d-f**, Transfer characteristics of the monolayer (**d**), bilayer (**e**), and trilayer (**f**) MoS₂ top-gated FETs at $V_{ds} = 0.5$ V in linear (blue line) and logarithmic (black line) scales. High on/off ratios of more than 10^8 are observed for all the devices. **g-i**, Output characteristics of the monolayer (**g**), bilayer (**h**), and trilayer (**i**) MoS₂ top-gated FETs at V_{ds} range from 0 to 1 V. The gate voltage V_g is from -2 V to 3 V with a step of 0.5 V for monolayer and trilayer devices and -1 V to 4 V with a step of 0.5 V for bilayer device. The linear behaviors of output curves indicating an ohmic-like contact between the graphite electrodes and the MoS₂ channel. The transfer and output characteristics of bilayer and trilayer FETs present one-order higher on-state current and improved contact than the monolayer FET.

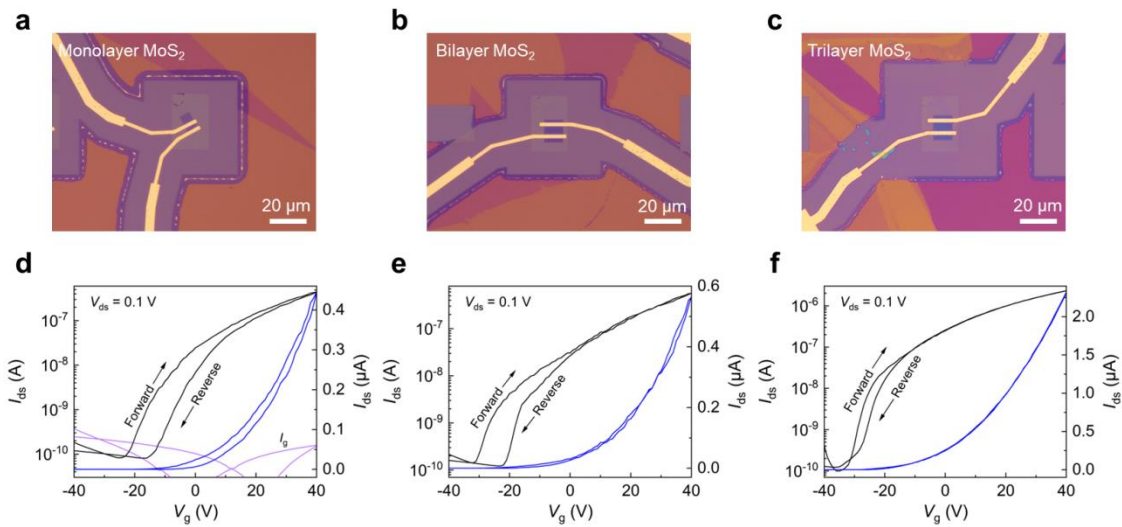


Figure S12. Electrical transport properties of monolayer, bilayer, and trilayer MoS₂ back-gated FETs fabricated directly on exfoliation substrates. **a-c**, Optical images of monolayer (**a**), bilayer (**b**), and trilayer (**c**) MoS₂ back-gated FETs. **d-f**, Transfer characteristics of the monolayer (**d**), bilayer (**e**), and trilayer (**f**) MoS₂ back-gated FETs at $V_{ds} = 0.1$ V in linear (blue line) and logarithmic (black line) scales. I_g represents the leakage current. The high leakage current may be caused by unavoidable damage to the substrates, which has undergone several EBL patterning steps, wet etching step of Au film, and dry etching step of MoS₂ flakes during the device fabrication process. The results demonstrate the feasibility of fabricating devices directly on exfoliation substrates.



Figure S13. Optical images taken at different stages of fabricating a $\sim 0.1^\circ$ twisted MoS_2 homobilayer sample. **a**, Two adjacent rectangular monolayer MoS_2 layers exfoliated on Au-patterned SiO_2 substrates. **b**, Two monolayer MoS_2 layers have been picked up by a PDMS/PPC/hBN stack. Distinct contrast is observed on the substrate before and after the pick-up of the monolayer MoS_2 . **c**, The fabricated $\sim 0.1^\circ$ twisted MoS_2 homobilayer sample on the PDMS/PPC/hBN stack.

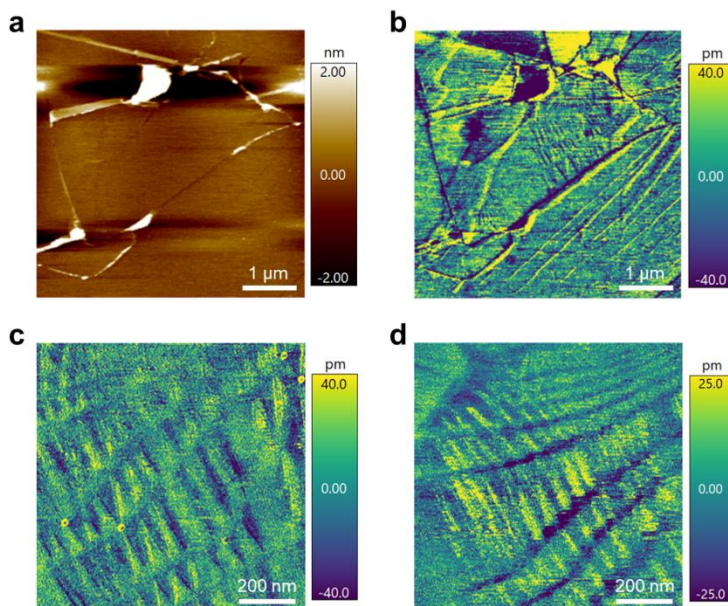


Figure S14. AFM height and PFM amplitude images of the $\sim 0.1^\circ$ twisted MoS_2 homobilayer sample. **a**, AFM height image of the $\sim 0.1^\circ$ twisted MoS_2 homobilayer sample. **b-d**, Large-scale and small-scale DART PFM amplitude images of the $\sim 0.1^\circ$ twisted MoS_2 homobilayer sample. Distorted moiré patterns are observed, with the period of about 100 - 200 nm. For moiré superlattices with such small twist angles,

the visualization of the moiré patterns is very challenging due to the large period and the significant atomic reconstruction.

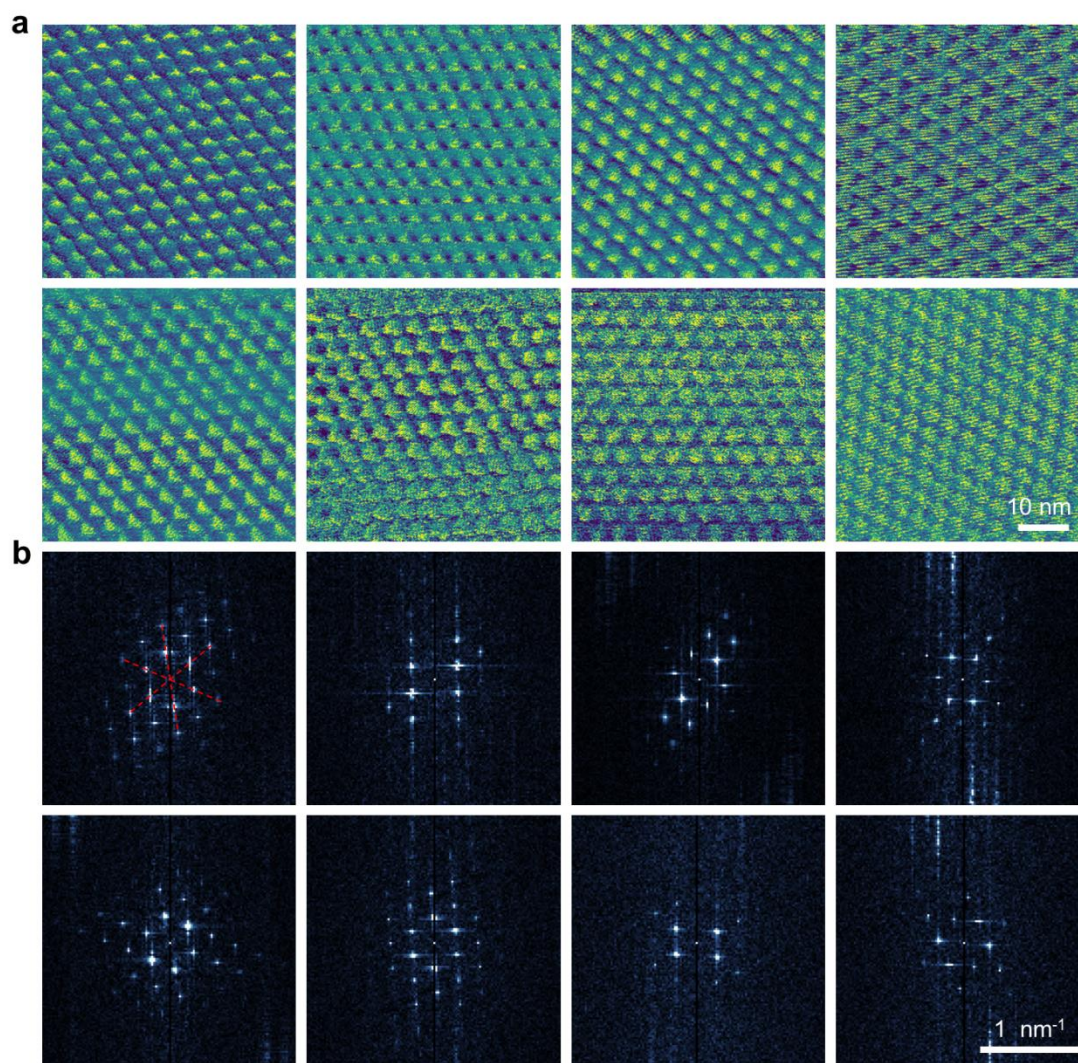


Figure S15. Moiré patterns visualized by PFM and corresponding fast Fourier transform (FFT) patterns of four 56° twisted MoS₂ homobilayer samples. a, PFM amplitude images at eight randomly selected positions of the four twisted MoS₂ homobilayer samples. **b**, FFT patterns at the eight randomly selected positions. Clear moiré patterns (a) and corresponding FFT patterns with six-fold symmetry (b) were observed at the eight randomly selected positions.

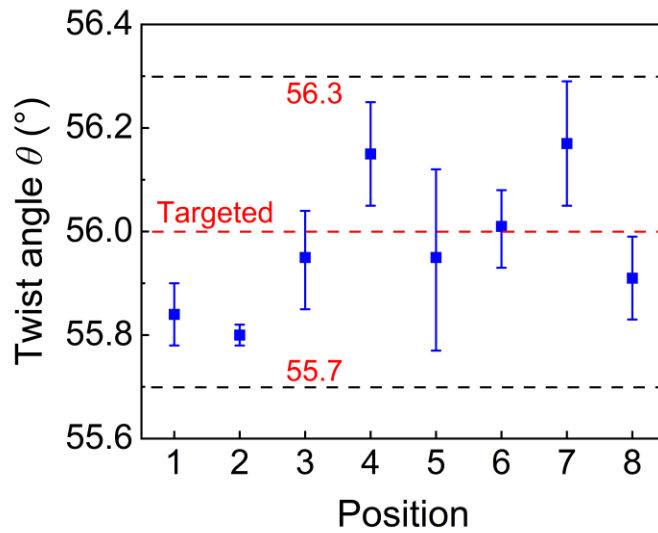


Figure S16. The twist angles at 8 positions of four twisted homobialyer MoS₂ samples with a 56° targeted twist angle extracted from corresponding FFT patterns. The angle-twisting accuracy is defined by comparing the measured twist angle with the targeted twist angle. The targeted twist angle is 56°, and the obtained twist angles are all within the range of 55.7-56.3°, indicating an angle-twisting accuracy of ~0.3° for the fabrication of twisted MoS₂ homobilayers.

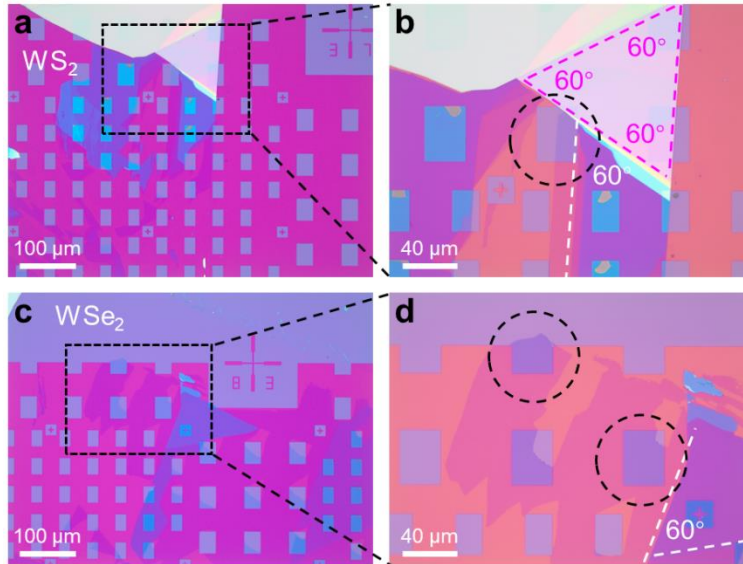


Figure S17. Optical images of mechanically exfoliated WS_2 and WSe_2 layers used for construction of twisted WS_2/WSe_2 moiré superlattices. **a,b**, Optical images of exfoliated WS_2 layers. The magenta and white dashed lines are aligned with the straight steps of the WS_2 layers, which are either parallel or at a 60° angle to each other. Therefore, we can use these straight steps to precisely represent the zigzag directions of the WS_2 layers. **c,d**, Optical images of exfoliated WSe_2 layers. Similar with WS_2 layers, straight steps are used to precisely represent the zigzag directions of the WSe_2 layers. Monolayer WS_2 (**b**) and WSe_2 (**d**) on rectangular SiO_2 substrates (marked by the black dashed circles) are adjacent to the straight steps and have the same crystal orientations with the determined zigzag directions.

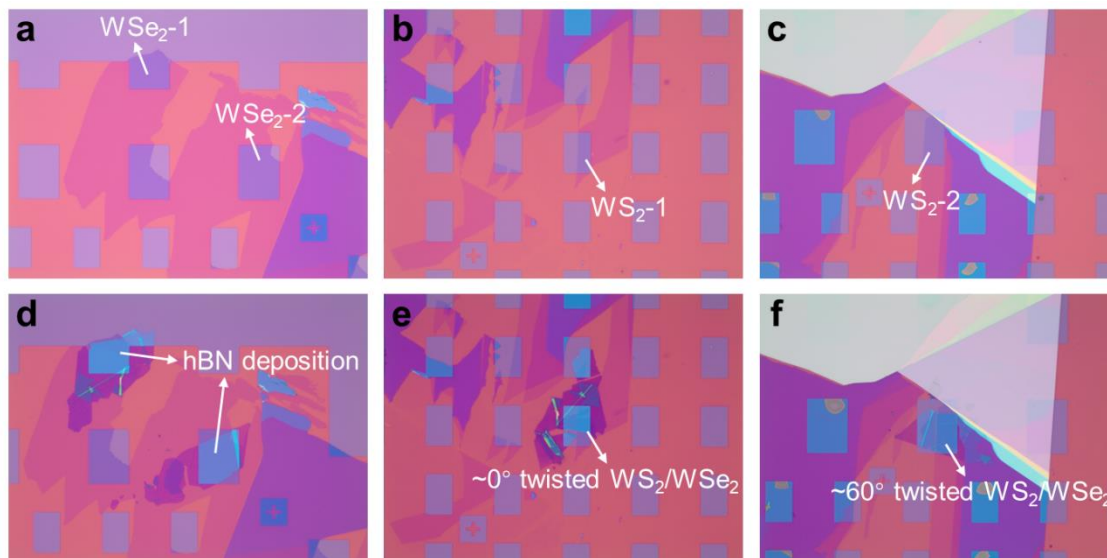


Figure S18. The simultaneous fabrication of the $\sim 0^\circ$ and $\sim 60^\circ$ twisted heterobilayer WS_2/WSe_2 . a-c, Optical images of mechanically exfoliated monolayer WSe_2 (a) and WS_2 (b,c) on Au-patterned SiO_2 substrates. Two adjacent WS_2 or WSe_2 flakes with the same determined zigzag directions are chosen for construction of the moiré superlattices. d, Optical image of the mechanically exfoliated monolayer WSe_2 after deposition of thin hBN layers. e,f, Optical images of the fabricated $\sim 0^\circ$ and $\sim 60^\circ$ twisted WS_2/WSe_2 moiré superlattices.

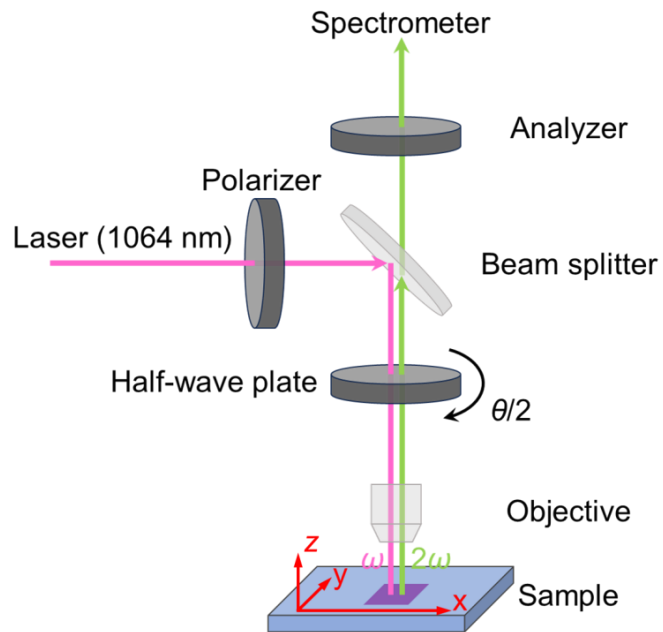


Figure S19. Illustration of the setup used for the polarization-resolved SHG characterizations and SHG spectroscopy. A laboratory coordinate system with x, y, and z axes are established. The initial laser polarization and the initial fast axis of half-wave plate are along the x axis. The half-wave plate rotates clockwise automatically during the measurements of polarization-resolved SHG.

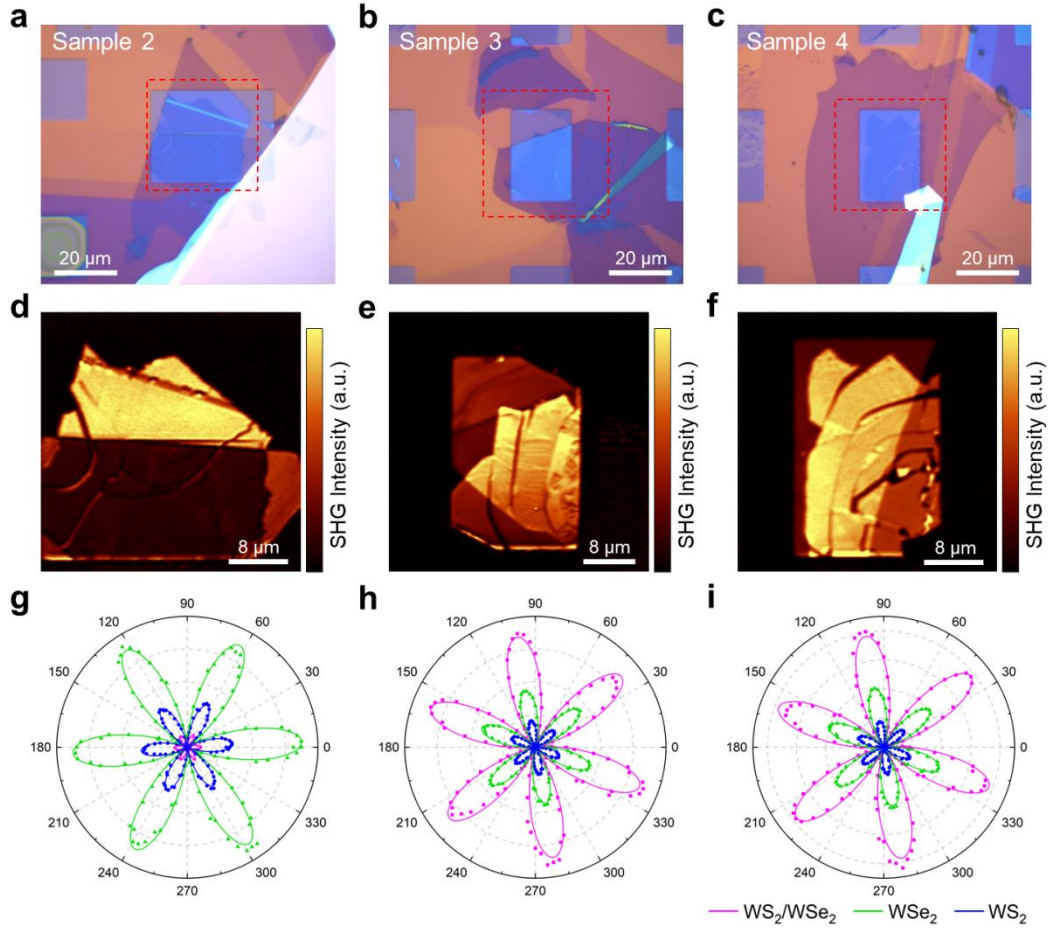


Figure S20. SHG mappings and polarization-resolved SHG characterizations of twisted heterobilayer WS₂/WSe₂ (sample 2-4). **a-c**, Optical images of ~0.5° (**a**), ~58.4° (**b**), and ~0° (**c**) twisted WS₂/WSe₂ heterobilayers on SiO₂ substrates with thin hBN as capping layers. **d-f**, The corresponding SHG mappings in areas marked by the red dashed square in (**a-c**). The twisted angles can be distinguished by considering whether the SHG signals are enhanced or suppressed at the overlapping heterobilayer regions compared to their monolayer counterparts. **g-i**, Polarization resolved SHG signals and the corresponding fittings of the twisted heterobilayer WS₂/WSe₂ (magenta symbol), the constituent monolayer WSe₂ (green symbol), and the constituent monolayer WS₂ (blue symbol) in sample 2-4.

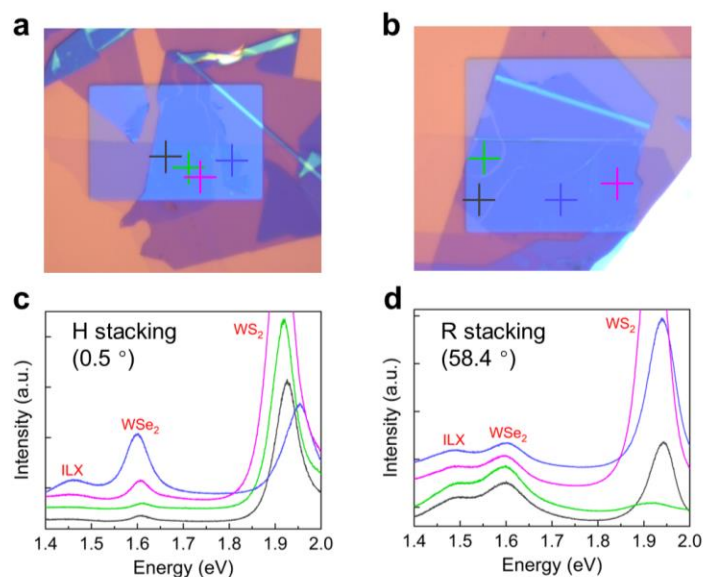


Figure S21. Interlayer exciton characterizations of twisted WS_2/WSe_2 moiré superlattices. **a,c**, Optical image (**a**) and PL spectra (**c**) of $\sim 0.5^\circ$ twisted WS_2/WSe_2 heterolayer (sample 1). The four spectra are obtained from four different locations marked by crosses in (**a**). Peak positions of interlayer excitons are ~ 1.46 eV. **b,d**, Optical image (**b**) and PL spectra (**d**) of $\sim 58.4^\circ$ twisted heterolayer WS_2/WSe_2 (sample 2). The four spectra are obtained from four different locations marked by crosses in (**b**). Peak positions of interlayer excitons are ~ 1.50 eV. The specific shapes and intensities of interlayer exciton peaks vary from location to location, which is consistent with previous reports^[4-6].

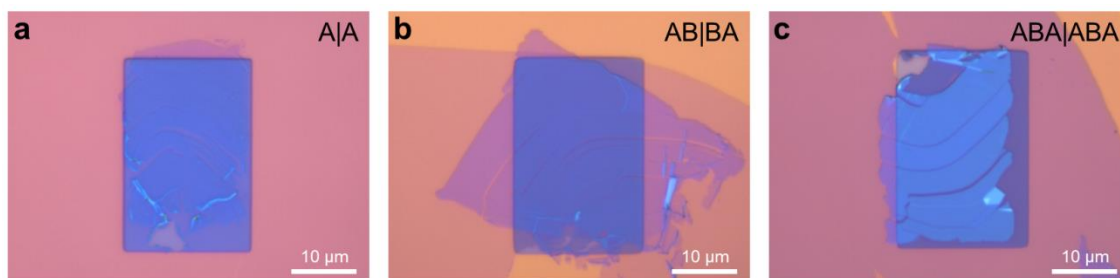


Figure S22. Optical images of the twisted multilayer MoS_2 superlattices for SHG spectra measurements. **a**, $\sim 0^\circ$ twisted bilayer MoS_2 (A|A). **b**, $\sim 60^\circ$ twisted four-layer MoS_2 (AB|BA). **c**, $\sim 0^\circ$ twisted six-layer MoS_2 (ABA|ABA).

Table S1. Comparisons of the PL peak, FWHM of previous reported WS₂, MoS₂, WSe₂, and MoSe₂ monolayers.

Samples	Preparation methods	Substrate	PL peak (eV)	FWHM (meV)	Reference
WS ₂	CVD	SiO ₂	1.96	60-70	[7]
WS ₂	CVD	SiO ₂	1.95	~44	[8]
WS ₂	Exfoliation	SiO ₂	1.93	38	This work
MoS ₂	CVD	Sapphire	1.88	56	[9]
MoS ₂	CVD	Glass	1.88	54	[10]
MoS ₂	CVD	Sapphire	1.88	56	[11]
MoS ₂	Exfoliation	SiO ₂	1.87	76	[12]
MoS ₂	Exfoliation	SiO ₂	1.84	~100	[13]
MoS ₂	Exfoliation	SiO ₂	1.82	53	This work
WSe ₂	Exfoliation	SiO ₂	1.65	~50	[13]
WSe ₂	Exfoliation	SiO ₂	1.64	~57	[14]
WSe ₂	Exfoliation	SiO ₂	1.61	53	This work
MoSe ₂	Exfoliation	SiO ₂	1.56	~50	[13]
MoSe ₂	CVD	SiO ₂	1.57	~62	[14]
MoSe ₂	Exfoliation	SiO ₂	1.57	~42	[14]
MoSe ₂	Exfoliation	SiO ₂	1.53	52	This work

Table S2. Comparisons of the layer-dependent superconducting transition temperature (T_c), residual resistance ratio (RRR), upper critical field (H_{c2}), and GL coherence length ($\xi(0)$) of few-layer NbSe₂.

Samples	$T_c(0.5R_N)$ (K)	$T_{c\text{-onset}}$ (K)	$T_{c\text{-zero}}$ (K)	ΔT (K)	RRR	$H_{c2}(0)$ (T)	$\xi_{GL}(0)$ (nm)
Bilayer	5.25	5.36	3.54	1.82	10.73	3.22 ± 0.04	10.1 ± 0.1
Trilayer	5.76	5.83	5.26	0.57	8.58	4.54 ± 0.10	8.5 ± 0.1
Five-layer	6.40	6.45	6.28	0.17	11.49	4.55 ± 0.07	8.5 ± 0.1
Bulk	6.81	6.86	6.71	0.15	13.61	5.94 ± 0.14	7.5 ± 0.1

Supplementary Note 1

Challenges in the fabrication process of moiré superlattices. To construct moiré superlattices, we need to pick up the exfoliated 2D layers using the PPC film as the transfer medium. During this process, we may encounter two challenges.

First, the insufficient adhesion force between PPC and hBN may lead to the failure of picking up the hBN/2D-layers stack on rectangular SiO₂, as the strong covalent-like interaction force between Au films and exfoliated 2D layers may impede the pick-up of hBN. We found that by using thick hBN with a thickness of 30-50 nm and by quickly lifting the PPC/hBN stack, the success rate of picking up the exfoliated 2D layers is significantly improved.

Second, due to the inevitable strain in the pick-up process and the strain at the edges of the rectangular monolayers, some cracks and wrinkles form (Figure S13c, Supporting Information), leading to a reduction in the lateral sizes of the uniform regions of the fabricated moiré superlattices to 10-20 μm .

Supplementary Note 2

Determination of the twist angles of the twisted MoS₂ homobilayer samples through fast Fourier transform (FFT) patterns. The lattice constant of MoS₂ is $a = 0.315$ nm. The moiré period λ for a twisted homobilayer sample is given by

$$\lambda = \frac{a}{\sqrt{2[1 - \cos(\theta)]}}$$

where ϑ is the twist angle. Considering the hexagonal crystal structure of MoS₂, the moiré period λ and the reciprocal vector λ^* satisfy the relationship of

$$\lambda = \frac{2}{\sqrt{3}\lambda^*}$$

Due to the inevitable strains along different directions, the moiré periods along each direction exhibited slight deviations. The reciprocal vector λ^* is directly measured from the FFT patterns with six-fold symmetry. From Figure S15b, three values of reciprocal vector (r_1 , r_2 , and r_3) along three directions marked by the three red dashed lines are obtained. For convenience, we define $\lambda_{\text{max}}^* = \text{maximum}(r_1, r_2, r_3)$, $\lambda_{\text{min}}^* = \text{minimum}(r_1, r_2, r_3)$. By solving the following two equations, we can get the maximum and minimum twist angles as ϑ_{max} and ϑ_{min} . The twist angle ϑ_a of each position is defined as the average of ϑ_{max} and ϑ_{min} . The error bar represents the difference between ϑ_a and $\vartheta_{\text{max}}/\vartheta_{\text{min}}$.

$$\frac{2}{\sqrt{3}\lambda_{\text{max}}^*} = \frac{a}{\sqrt{2[1 - \cos(\vartheta_{\text{max}})]}}$$

$$\frac{2}{\sqrt{3}\lambda_{\text{min}}^*} = \frac{a}{\sqrt{2[1 - \cos(\vartheta_{\text{min}})]}}$$

Supplementary Note 3

The concept of using a hybrid of high- and low-adhesion surface to exfoliate 2D crystals. During the review process of this manuscript, we noticed another paper reported the adhesive matrix method^[15] that provide the concept of using a hybrid of high- and low-adhesion surface to exfoliate 2D crystals. Actually, this concept is consistent with our method of utilizing the Au-template substrate, where the adhesion of SiO₂ is low and that of Au films is high. What's more, our Au-template-assisted exfoliation method has some advantages over the adhesive matrix method.

First, the universality of our Au-template-assisted exfoliation is higher than that of the adhesive matrix transfer method. As shown in Figure 1 and Figure S4 (Supporting Information), we have exfoliated fourteen specific 2D materials using our Au-template-assisted exfoliation method, whereas the adhesive matrix transfer method is only limited to four specific 2D materials (MoS₂, WSe₂, PtS₂ and GaS).

Second, the feature sizes of 2D materials on low-adhesive surface achieved by our Au-template-assisted exfoliation method are larger than that by the adhesive matrix transfer method. Figures S2h and Figure S3f display the exfoliation results using our Au-patterned SiO₂ substrates, while Figures 1f^[15] and Figure S1b^[15] show the exfoliation results using the adhesive matrix transfer method. The area of each SiO₂ rectangle with feature sizes of 30×40 μm² achieved by our method is nearly 20 times larger than the area of 8-μm-width squares or circles achieved by the adhesive matrix transfer method. Compared with the adhesive matrix transfer method, using our Au-template-assisted exfoliation method, the area of the low-adhesion surface is significant increased, while the exfoliation can still reach ~60% high, similar to that using the adhesive matrix transfer method.

Third, the unique capability for efficient and precise alignment of moiré superlattices enabled by our Au-template-assisted exfoliation method. While the adhesive matrix transfer method demonstrates the ability of aligned fabrication of van der Waals heterostructures, it is only limited to aligned monolayer-graphene/gold heterostructures and suspended double-layer graphene. In contrast, our method shows significant advantages in efficiently and precisely fabricating various moiré superlattices, including twisted homobilayers, twisted heterobilayers, and twisted multilayer structures.

References

- [1] H. Li, J. Wu, X. Huang, G. Lu, J. Yang, X. Lu, Q. Xiong, H. Zhang, *ACS Nano* **2013**, 7, 10344.
- [2] X. Xi, L. Zhao, Z. Wang, H. Berger, L. Forró, J. Shan, K. F. Mak, *Nat. Nanotechnol.* **2015**, 10, 765.
- [3] A. Favron, E. Gauffrès, F. Fossard, A.-L. Phaneuf-L'Heureux, N. Y. W. Tang, P. L. Lévesque, A. Loiseau, R. Leonelli, S. Francoeur, R. Martel, *Nat. Mater.* **2015**, 14, 826.
- [4] K. L. Seyler, P. Rivera, H. Yu, N. P. Wilson, E. L. Ray, D. G. Mandrus, J. Yan, W. Yao, X. Xu, *Nature* **2019**, 567, 66.
- [5] K. Tran, G. Moody, F. Wu, X. Lu, J. Choi, K. Kim, A. Rai, D. A. Sanchez, J. Quan, A. Singh, J. Embley, A. Zepeda, M. Campbell, T. Autry, T. Taniguchi, K. Watanabe, N. Lu, S. K. Banerjee, K. L. Silverman, S. Kim, E. Tutuc, L. Yang, A. H. MacDonald, X. Li, *Nature* **2019**, 567, 71.
- [6] F. Liu, W. Wu, Y. Bai, S. H. Chae, Q. Li, J. Wang, J. Hone, X. Y. Zhu, *Science* **2020**, 367, 903.
- [7] Z. Xu, Y. Lv, J. Li, F. Huang, P. Nie, S. Zhang, S. Zhao, S. Zhao, G. Wei, *RSC Advances* **2019**, 9, 29628.
- [8] J. Zhang, L. Du, S. Feng, R.-W. Zhang, B. Cao, C. Zou, Y. Chen, M. Liao, B. Zhang, S. A. Yang, G. Zhang, T. Yu, *Nat. Commun.* **2019**, 10, 4226.
- [9] T. Li, W. Guo, L. Ma, W. Li, Z. Yu, Z. Han, S. Gao, L. Liu, D. Fan, Z. Wang, Y. Yang, W. Lin, Z. Luo, X. Chen, N. Dai, X. Tu, D. Pan, Y. Yao, P. Wang, Y. Nie, J. Wang, Y. Shi, X. Wang, *Nat. Nanotechnol.* **2021**, 16, 1201.
- [10] P. Yang, X. Zou, Z. Zhang, M. Hong, J. Shi, S. Chen, J. Shu, L. Zhao, S. Jiang, X. Zhou, Y. Huan, C. Xie, P. Gao, Q. Chen, Q. Zhang, Z. Liu, Y. Zhang, *Nat. Commun.* **2018**, 9, 979.
- [11] Q. Wang, N. Li, J. Tang, J. Zhu, Q. Zhang, Q. Jia, Y. Lu, Z. Wei, H. Yu, Y. Zhao, Y. Guo, L. Gu, G. Sun, W. Yang, R. Yang, D. Shi, G. Zhang, *Nano Lett.* **2020**, 20, 7193.
- [12] D. Sercombe, S. Schwarz, O. D. Pozo-Zamudio, F. Liu, B. J. Robinson, E. A. Chekhovich, I. I. Tartakovskii, O. Kolosov, A. I. Tartakovskii, *Sci. Rep.* **2013**, 3, 3489.
- [13] S. Tongay, J. Suh, C. Ataca, W. Fan, A. Luce, J. S. Kang, J. Liu, C. Ko, R. Raghunathanan, J. Zhou, F. Ogletree, J. Li, J. C. Grossman, J. Wu, *Sci. Rep.* **2013**, 3, 2657.
- [14] H. Fang, C. Battaglia, C. Carraro, S. Nemsak, B. Ozdol, J. S. Kang, H. A. Bechtel, S. B. Desai, F. Kronast, A. A. Unal, G. Conti, C. Conlon, G. K. Palsson, M. C. Martin, A. M. Minor, C. S. Fadley, E. Yablonovitch, R. Maboudian, A. Javey, *Proc. Natl Acad. Sci. USA* **2014**, 111, 6198.

[15] P. F. Satterthwaite, W. Zhu, P. Jastrzebska-Perfect, M. Tang, S. O. Spector, H. Gao, H. Kitadai, A.-Y. Lu, Q. Tan, S.-Y. Tang, Y.-L. Chueh, C.-N. Kuo, C. S. Lue, J. Kong, X. Ling, F. Niroui, *Nat. Electron.* **2024**, *7*, 17.